Identification of a functional point defect in SrTiO_{3}

Daesu Lee, Hongwei Wang, Brenton A. Noesges, Thaddeus J. Asel, Jinbo Pan, Jung-Woo Lee, Qimin Yan, Leonard J. Brillson, Xifan Wu, and Chang-Beom Eom

Phys. Rev. Materials **2**, 060403 — Published 21 June 2018

DOI: 10.1103/PhysRevMaterials.2.060403

Identification of a functional point defect in $SrTiO_3$

Daesu Lee,[1,†] Hongwei Wang,[2,†] Brenton A. Noesges,[3,†] Thaddeus Asel,[3] Jinbo Pan,[2] Jung-Woo Lee[1], Qimin Yan,[2] Leonard Brillson,[3] Xifan Wu,[2] and Chang-Beom Eom[1,*]

[1]*Department of Materials Science and Engineering, University of Wisconsin–Madison, Madison, Wisconsin 53706, USA.*
[2]*Department of Physics, Temple University, Philadelphia, Pennsylvania 19122, USA.*
[3]*Department of Electrical and Computer Engineering and Department of Physics, The Ohio State University, Columbus, Ohio 43210, USA*

Unveiling both the presence and nature of point defects is one of the biggest challenges in condensed matter physics and materials science. Particularly in complex oxides, even a minute amount of unavoidable point defects could generate novel physical phenomena and functions, such as visible light emission and ferroelectricity, yet it remains elusive to clearly identify such point defects. Here, taking $SrTiO_3$ as a model system, we show that iterative feedback among atomic-layer and stoichiometry-controlled thin-film epitaxy, hybrid density functional theory, and high-resolution cathodoluminescence spectroscopy allows for the identification of a functional cationic defect – the Ti antisite (Ti_{Sr}) defect. Our cathodoluminescence measurements reveal sub-band-gap luminescence, whose spectral fine structures show excellent quantitative agreement, as well as one-to-one correspondence, with the theoretically predicted optical transitions from intrinsic point defects like Ti_{Sr}. Guided by the theory and spectroscopic results, we also control a cation stoichiometry, and it in turn results in good systematics in cathodoluminescence spectra. Not limited to the identification of Ti_{Sr}, this approach allows for more reliable, self-consistent defect study, and provides critical insight into a microscopic picture of point defects in complex oxides.

---

[*] e-mail: eom@engr.wisc.edu

[†] These authors contributed equally to this work.

I. INTRODUCTION

Point defects are universally present in every material, and significantly affect physical properties and functions of materials [1–4]. In complex oxides, point defects have played a critical role in determining structural, electronic, optical, and electrochemical properties, especially via modifying the charge, spin, and orbital states of cations (e.g., transition metal ions). Recent advances in growth techniques for complex oxides have enabled control of film stoichiometry to achieve highly pure materials with intrinsic bulk properties [5]. On the other hand, it has been also found that point defects can generate a broad spectrum of physical properties, including superconductivity [6], ferroelectricity [7–9], metal-insulator transition [10], and emergent phenomena [11] in complex oxides. To date, it has been believed that most of the above emergent functions originate from oxygen vacancies, and the roles played by other intrinsic defects (e.g., cation vacancy and related defects) have been largely neglected.

$SrTiO_3$ is one of the most important and interesting complex oxides [12]. A pure, unstrained $SrTiO_3$ has a simple perovskite cubic structure at room temperature and is a nonmagnetic, paraelectric band insulator with an indirect band gap of ~3.2 eV [13]. Interestingly, an external perturbation, such as epitaxial strain and doping, has been employed to realize a wide range of physical properties and functions in $SrTiO_3$. In addition to this intentional engineering, even small concentrations of unavoidable point defects can play a decisive role in the properties of $SrTiO_3$. Strontium and oxygen vacancies have been considered to be two dominant point defects in $SrTiO_3$, because of their small formation energy [14,15]. While the Sr vacancy (V_{Sr}) can act to trap carriers and limit carrier mobilities [16], the oxygen vacancy (V_{O}) is considered to induce superconductivity [17] and *n*-type conductivity [18,19] in $SrTiO_3$. In addition to V_{Sr} and

V_O, recent works propose that antisite Ti defect (Ti_{Sr}), where a Sr is replaced by a Ti atom (Fig. 1(a)), should also be intrinsically present and could lead to interesting and technologically important phenomena [7,9], such as visible light emission and ferroelectricity. However, it still remains elusive to unambiguously identify these point defects.

Cathodoluminescence (CL) spectroscopy has been one of the most successful techniques for characterizing defects in a material [20,21]. Besides near-band-gap and higher lying energy transitions in semiconductors and insulators, luminescence at energies below the band gap arises from defect levels located in the band gap. In a simple material, the measured defect levels give rather straightforward evidence, from which we can identify point defects in the material. In contrast, a complicated structural and electronic reconstruction can occur due to point defects in complex oxides, which necessitates additional theoretical support. Although density functional theory (DFT) has been widely used to explore the electronic structure of complex oxides, its calculated band gap shows a quantitative mismatch with the experimental value [22,23]. This well-known band gap problem has made it impossible to precisely compare the measured and calculated defect-induced optical transitions and identify the relevant point defects. Recently, a more reliable approach, that is, the Heyd, Scuseria, and Ernzerhof (HSE) hybrid functional [24,25], has been adopted in this field. The accuracy of HSE in predicting physical properties for $SrTiO_3$ has already been established [26,33], by reproducing not only the experimental band gap but also dielectric properties and the equilibrium crystal volume.

Here, using iterative feedback loops among atomic-layer- and stoichiometry-controlled thin film epitaxy, hybrid density functional theory, and CL spectroscopy, we identify a functional point defect – Ti antisite (Ti_{Sr}) defect – in a complex oxide $SrTiO_3$. Perovskite oxides usually have multiple intrinsic point defects, such as Ti_{Sr}, V_{Sr}, and V_O (Fig. 1), which can contribute to the emergence of functional properties in $SrTiO_3$. Notably, those point defects not only can show distinct dielectric functions, but also can generate spectroscopically resolvable optical transitions. Therefore, by precisely calculating the defect-induced optical transitions and performing high-resolution CL measurements for the controlled thin films, we successfully identify all the measured sub-band-gap optical transitions from point defects and confirm the presence of a functional cationic defect, i.e., Ti_{Sr}, in $SrTiO_3$.

II. EXPERIMENTAL AND THEORETICAL METHODS

Homoepitaxial $SrTiO_3$ thin films were grown on (001) $SrTiO_3$ substrate using the pulsed laser deposition (PLD) method. Before deposition, low miscut (< 0.05°) $SrTiO_3$ substrates were treated with a buffered hydrofluoric acid etch and annealed in oxygen at 1050° C for 6 hours to create atomically smooth single TiO_2 terminated surfaces with unit cell steps. A KrF excimer laser (248 nm) beam was focused on $SrTiO_3$ single-crystal targets to an energy density of ~2.0 J/cm^2 and pulsed at 5 Hz. $SrTiO_3$ films were grown at a substrate temperature of 750 °C and oxygen partial pressures of 10 mTorr. The PLD system was equipped with high-pressure reflection high-energy electron diffraction (RHEED), which enabled atomic-layer-controlled growth and *in situ* monitoring during the growth [Fig. 2(a)]. After growth, the films were annealed in 1 atmosphere of oxygen during cooling. The crystal structure of the films was determined using a high-resolution four-circle X-ray diffraction (XRD) machine (Bruker D8 advance). The surface of films was atomically smooth with single unit-cell height steps measured by atomic force microscopy (AFM), as shown in Fig. 2(b).

For first-principles calculations, $SrTiO_3$ is modeled by a supercell of 160 atoms, constructed by the $2 \times 2 \times 2$ repetition of the 20-atom unit cell [27], which accommodates the octahedral rotation [28]. One defect is then generated within the 160-atom supercell for each of three types of defects of $\mathrm{Ti}_{\mathrm{Sr}}$, V_{Sr}, and V_{O}. For defects modeled in large supercells, the interaction between periodic images is small and can be neglected. Our first-principles calculations are based on the generalized Kohn-Sham density functional theory (DFT) with the screened hybrid functional HSE06 [24,25]. The structure optimizations have been performed by the CRYSTAL14 code package [29] that employs a linear combination (contraction) of localized Gaussian type functions to represent the Bloch orbitals. The Hay-Wadt effective core potentials [30] have been adopted for Ti and Sr atoms, which replace only inner core orbitals with the effective potentials but orbitals for valence electrons are calculated self-consistently. The light oxygen atoms have been described by all-electron basis sets. The basis sets have been chosen following literature [31]: O-8-411(1d)G, Ti-411(311d)G and Sr-311(1d)G, where the numbers refer to the level of contraction. The integrations over the Brillouin zone were performed with a Γ-centered 2 × 2 × 2 k-point mesh. The self-consistent field convergences threshold on energy is set to be 10^{-8} Hartree. The structure is considered to be relaxed when 3×10^{-5} Hartree/Bohr in the root-mean-square values of forces and 1.2×10^{-4} Bohr in the root-mean-square values of atomic displacements are simultaneously achieved for atomic position and lattice constant optimizations respectively. With the relaxed structures for each defect modeled in the $SrTiO_3$ supercell, we use DFT as implemented in VASP [32] code package to identify the energies of the optical spectra. The formation energy of the $\mathrm{Ti}_{\mathrm{Sr}}$ in a charge state q can be calculated by: $E^f(\mathrm{Ti}_{\mathrm{Sr}}) = E_T(\mathrm{Ti}_{\mathrm{Sr}}) - E_T(\mathrm{SrTiO_3}) - \mu_{\mathrm{Sr}} + \mu_{\mathrm{Ti}} + q(\varepsilon_{\mathrm{VBM}} + E_{\mathrm{F}}) + \Delta$, where $E_{\mathrm{T}}(\mathrm{SrTiO_3})$ is the total energy of a perfect $SrTiO_3$ crystal system and $E_{\mathrm{T}}(\mathrm{Ti}_{\mathrm{Sr}})$ is the total energy of the supercell containing an $\mathrm{Ti}_{\mathrm{Sr}}$ in a charge state q. The atom X that is removed from the crystal is placed in a reservoir of energy μ_X, referenced to the total energy (per atom) of the standard phase. The reference of Fermi level E_{F} is the energy at valence-band maximum (VBM) $\varepsilon_{\mathrm{VBM}}$ of $SrTiO_3$ representing the energy of the electron reservoir. Δ is the charge-state dependent finite-size correction [33]. To be consistent with previous work [34], we set $\mu_{\mathrm{Ti}} = -4.0$ eV and $\mu_{\mathrm{Sr}} = -3.4$ eV. Note that this choice does not affect the position of thermodynamic transition levels, which correspond to the Fermi-level positions where formation energies of different charge states cross and the charge state of defect changes.

Depth-resolved cathodoluminescence spectroscopy (DR-CLS) was performed using a Physical Electronics Inc. (PHI) 110-10 glancing incidence election gun operated with beam voltages from 0.5 kV to 4.5 kV and an emission current controlled to provide a constant power of 1 mW with varying voltages under ultrahigh vacuum (UHV) conditions. The emitted photons were collected by a CaF_2 lens in vacuum, passed through a sapphire window port of the UHV chamber into an Oriel F-number matcher. The collected light was then dispersed through an Oriel MS260i monochromator using a grating with a 300 nm blaze into an Andor iDus OE charge coupled detector (CCD). To minimize charging by the incident electron beam, the sample was covered with a copper grid that was rinsed with acetone, methanol, isopropanol and then DI water prior to use. Individual DRCL spectra were separated by 10 min. periods sufficient to discharge any trapped charge. The electron gun's orientation prevented sample illumination by the filament glow. The normalized 1.8 eV and 2.1 eV peak intensities shown in Fig. 5(b) are defined as the intensity ratio between these CLS peaks and the near-band-edge peak at 3.6 eV [35].

III. RESULTS AND DISCUSSION

Figure 2(c) shows XRD θ–2θ scan of our sample around the $SrTiO_3$ (002) Bragg peak. The XRD peak position of the $SrTiO_3$ film was almost identical with that of the $SrTiO_3$ substrate, indicating that our $SrTiO_3$ film had a normal unit-cell volume (with a small expansion of <0.1%) and was free of excessive point defects. Based on the measured lattice volume, we may expect that physical properties of the film would be quite similar to those of pure $SrTiO_3$ bulk. Our previous Raman spectroscopy measurements, however, revealed that our films are polar with the nonpolar-to-polar transition temperature at ~400 K [8,36], whereas pure $SrTiO_3$ bulk is nonpolar at every temperature. Furthermore, our electrical measurements showed room-temperature ferroelectricity in our ultrathin $SrTiO_3$ homoepitaxial films [9]. Regarding the distinct Raman spectra of Sr-deficient and Ti-deficient $SrTiO_3$ [36], we found our films to be Sr-deficient, which was also confirmed by a chemical composition analysis like wave-length dispersive X-ray spectroscopy [8]. This indicates the presence of a Sr-deficiency-related defect that generates ferroelectricity in our nominally stoichiometric $SrTiO_3$ films.

In the case of Sr-deficient $SrTiO_3$, our first-principles calculation shows that Ti_{Sr} is the only the point defect that can generate polar distortion [9]. Figure 1 shows the calculated local atomic distortions at the vicinity of three representative intrinsic defects – Ti_{Sr}, V_O^{+1}, and V_{Sr}^{-1}, modeled in a large $SrTiO_3$ supercell. Among these three types of defects, Ti_{Sr} is only the point defect that breaks the inversion symmetry, generating a large electric dipole. The broken inversion symmetry is facilitated by an electronic reconstruction induced by Ti_{Sr}. The total energy is significantly lowered by the electronic hybridization between the Ti-*3d* states and the O-*2p* electronic states. Atomic reconstructions occur consequently, which can be clearly seen by the Ti_{Sr} forming relatively stronger Ti-O bonds with six of the oxygen atom, while moving away from the other rest six oxygen atoms in its first coordination shell, as presented in Fig. 1(a). Such a drastic atomic reconstruction generates an electric dipole around 10 e·Å in our first-principles calculations, which is significantly larger than that in a conventional ferroelectric $BaTiO_3$ of 1.3 e·Å.

On the other hand, due to the featureless nature of the electronic structure of charged vacancies, a V_{Sr}^{-1} or V_O^{+1} defect doesn't introduce any abrupt electronic reconstruction in $SrTiO_3$. The atoms surrounding these charged vacancies respond to an electrostatic interaction from the defect. The resulting local atomic structures are distorted away from the original cubic symmetry, however, rather isotopically. Not surprisingly, the inversion symmetries are preserved and no local electric dipole is generated in both types of vacancies, as seen in Fig. 2(b) and (c). It should be noted that we theoretically examined all the possible point defects and their clusters in the case of Sr-deficient $SrTiO_3$, and found that only the Ti_{Sr} induces a stable switchable polarization [9], a prerequisite for ferroelectricity.

Interestingly, our calculation also revealed that Ti_{Sr} induces local oxygen-octahedral tilts, as well as local polarization (Fig. 1). While these octahedral tilts can mainly change the local crystal shape, the overall crystal volume might remain almost preserved. The crystal volume change in $SrTiO_3$ with Ti_{Sr} was calculated as small as ~0.3%, compared to that of stoichiometric $SrTiO_3$, and it will be even smaller when the calculated cell size is sufficiently large. Notably, the crystal volume was decreased by Ti_{Sr}, rather than being increased. Therefore, according to our calculations, Ti_{Sr} can generate polar distortion, but doesn't induce excessive crystal volume change, consistent with our XRD, Raman, and electrical measurements.

For the next step, we theoretically examined the optical transition from Ti_{Sr} for checking if it is optically detectable. Assuming that Ti_{Sr} initially exists in +1 charge state (i.e., Ti_{Sr}^{+1}), the localized electron in the defect state can recombine with a hole in the valence band, the latter of which is generated by the electron-hole excitation process of the experiment. Following the above process, the Ti_{Sr}^{+1} is converted to +2 charge state (i.e., Ti_{Sr}^{+2}), as described by $Ti_{Sr}^{+1} + h \rightarrow Ti_{Sr}^{+2}$, emitting photons simultaneously. When the Fermi level is below 2.6 eV above the VBM, there is a possibility that Ti_{Sr} mainly exists in +2 charge state. In this case, the electron can be excited from the valence band to the empty defect state during optical excitation and generate a +1 charge state, thus allowing the same optical emission process $Ti_{Sr}^{+1} + h \rightarrow Ti_{Sr}^{+2}$. Theoretically, the above optical spectra can be determined by the thermodynamic transition level as well as the correction considering the Stokes shifts. As shown in Fig. 3(a), the thermodynamic transition level between Ti_{Sr}^{+2} and Ti_{Sr}^{+1} states is revealed to be 2.6 eV above the VBM from our first-principles calculations based on hybrid density functional theory. Compared with the GGA+U results with the ad-hoc band gap correction in Ref. 7, the (2+/+) transition level for the Ti antisite defect is shifted from 2.13 eV above the VBM in Ref. 7 to 2.6 eV above the VBM by our HSE calculations. We believe that HSE provides a more reliable description of the electronic structure in order to determine the transition levels and corresponding optical signatures. The characteristic time of lattice relaxation is much longer than that of the electron-hole excitations. Therefore, the local atomic structure can be assumed to be intact during the optical process according to the Frank-Condon principle. This physical principle allows us to predict the optical transition associated with Ti_{Sr} to be at 1.74 eV, with the computed Stokes shift of 0.86 eV, as schematically shown by our configuration coordinate diagram in Fig. 3(b). By the same token, the optical transitions at 2.80 and 2.03 eV have been predicted to be associated with oxygen vacancy of +1 charge state (i.e., V_O^{+1}) and Sr vacancy of –1 charge state (i.e., V_{Sr}^{-1}), respectively, which are also consistent with recent calculations [34].

In order to measure those point-defect-induced optical transitions, we carried out the CL measurements for nominally stoichiometric $SrTiO_3$ and slightly Sr-deficient $Sr_{0.99}TiO_3$ thin films, as shown in Fig. 4(a). Importantly, we were able to achieve high depth resolution by a differential technique, subtracting suitably normalized spectra acquired at lower energy from slightly higher energy spectra [37]. The measured CL data exhibits the spectral fine structures with multiple peaks at ~1.6, ~1.8, ~2.1, and ~2.9 eV, which are more obvious in $Sr_{0.99}TiO_3$ (lower panel in Fig. 4(a)), along with broad signals at 2.3–2.6 eV due to V_O-related defects [37]. Other strong peaks at ~3.6 and ~4.1 eV correspond to the direct-band-gap emission and above-band-gap emission from Ti t_{2g} orbitals [34], respectively. All these measured peak energies are in excellent agreement with our theoretical calculations. Figure 4(b) illustrates the optical transitions, either predicted from first-principles calculations or taken from the literatures [38], showing 1.60, 1.74, 2.03, and 2.80 eV optical transitions by Ti^{3+}, Ti_{Sr}^{+1}, V_{Sr}^{-1}, and V_O^{+2}, respectively. Therefore, based on this quantitative agreement, as well as one-to-one correspondence, between theoretical and experimental data, we could effectively evidence the presence of several point defects, including the functional Ti_{Sr}, in $SrTiO_3$ thin films.

Note that positively charged Ti_{Sr} can couple with negatively charged V_O through the attractive Coulomb interaction to form defect complexes. However, this does not rule out the existence of isolated defects and their corresponding optical peaks. Furthermore, as studied in Ref. 7, the Ti_{Sr}-V_O complexes are predicted to exhibit optical absorption and emission peaks at energies that are close to what are induced by the isolated Ti_{Sr}. This supports that the optical transition at ~1.8 eV could originate from the Ti_{Sr}-related defect, not depending on whether it is isolated or forms a complex with V_O.

Defect energy levels are often located closely, making it challenging to assign the defects unambiguously, only by using the theory and spectroscopic measurement. For example, we found that in nominally stoichiometric $SrTiO_3$ films (upper panel in Fig. 4(a)), the 1.6-eV CL peak by Ti^{3+} is dominant and can mask the signals from other point defects, especially, from Ti_{Sr} at ~1.8 eV. Although pure $SrTiO_3$ is an insulator, oxygen vacancies can introduce free electrons, resulting in Ti^{3+} neighboring sites and associated luminescence at ~1.6 eV [38]. Precise control of the oxygen vacancy concentration in $SrTiO_3$ is difficult, resulting in large variations of both the 1.6-eV Ti^{3+}-related and 2.9 eV V_O-related CL peaks. However, deposition of $SrTiO_3$ with carefully controlled stoichiometry could permit us to vary the concentration of these defects, demonstrating our ability to tune the 1.6-eV and other defect-mediated CL peaks in $SrTiO_3$ systematically. This systematics in CL spectra would allow for more reliable defect assignment.

For such systematic study, we performed CL measurements for $Sr_{1-x}TiO_3$ thin films with the controlled Sr deficiency. We prepared four systematic $Sr_{1-x}TiO_3$ samples (x ~ 0.00, 0.005, 0.01, and 0.02) [27], using the same $SrTiO_3$ substrate that was cut into smaller pieces for the film growth. Importantly, based on our DFT calculations [27], we controlled the Sr deficiency in our samples to be below $x = 0.06$, where we could treat a defect as being isolated. In contrast to donor-like V_O, V_{Sr} can act as an electron acceptor, so it can suppress the formation of Ti^{3+}. Figure 5(a) shows the CL spectra for $SrTiO_3$, $Sr_{0.995}TiO_3$, $Sr_{0.99}TiO_3$, and $Sr_{0.98}TiO_3$, where the data of $SrTiO_3$ and $Sr_{0.99}TiO_3$ are identical to those in Fig. 4(a). With the increase of Sr deficiency, the 1.6-eV CL peak becomes suppressed, whereas the 1.8-eV and 2.1-eV CL peaks become enhanced. We quantitatively analyzed the enhancement of 1.8-eV and 2.1-eV CL peaks for larger Sr deficiency (Fig. 5(b)), by normalizing their peak area with that of the band-gap emission at ~3.6 eV. While $Sr_{0.995}TiO_3$ shows a slightly decreased 2.1-eV peak area, possibly due to filling of any A-site vacancies with Ti, both 1.8-eV and 2.1-eV peaks show general enhancement with the increased Sr deficiency. This systematic change is consistent with our understanding that 1.6-eV, 1.8-eV, and 2.1-eV CL peaks come from Ti^{3+}, Ti_{Sr}, and V_{Sr}, respectively.

IV. CONCLUSION

In summary, we have identified a functional cationic defect, i.e., Ti_{Sr}, in $SrTiO_3$, using a combination of atomic-layer- and stoichiometry-controlled thin-film epitaxy, hybrid density functional calculation, and high-resolution CL measurement. All the measured sub-band-gap luminescence could be assigned to the optical transitions from point defects like Ti_{Sr}, with excellent quantitative agreement with theoretical predictions. We also demonstrated that spectral fine structures in the defect-induced luminescence could be systematically tuned, for example, by theory-guided, intentional control of cationic stoichiometry. Our study allows better microscopic understanding on how a point defect contributes to the optical transitions, and guides us to effectively identify the point defect in complex oxides. Our methodology described here is not limited to $SrTiO_3$, but will be generally applicable to other complex oxides and materials for identifying and utilizing functional point defects. It should be also of great interest to directly visualize the functional cationic defects in complex oxides, e.g., by using transmission electron microscopy [39].

ACKNOWLEDGEMENTS

This work was supported by funding from the DOE Office of Basic Energy Sciences under award number DE-FG02-06ER46327. The work at Temple University was partially supported as part of the Center for the Computational Design of Functional Layered Materials, an Energy

Frontier Research Center funded by the U.S. Department of Energy, Office of Science, Basic Energy Sciences under Award No. DE-SC0012575 (H.W. and X.W. carried out the defect calculations and analysis).

REFERENCES

[1] S. Aggarwal and R. Ramesh, *Point Defect Chemistry of Metal Oxide Heterostructures*, Annu. Rev. Mater. Sci. **28**, 463 (1998).

[2] H. L. Tuller and S. R. Bishop, *Point Defects in Oxides: Tailoring Materials through Defect Engineering*, Annu. Rev. Mater. Res. **41**, 369 (2011).

[3] N. Poccia, M. Fratini, A. Ricci, G. Campi, L. Barba, A. Vittorini-Orgeas, G. Bianconi, G. Aeppli, and A. Bianconi, *Evolution and Control of Oxygen Order in a Cuprate Superconductor*, Nat. Mater. **10**, 733 (2011).

[4] S. V. Kalinin and N. A. Spaldin, *Functional Ion Defects in Transition Metal Oxides*, Science **341**, 858 (2013).

[5] D. G. Schlom, *Perspective: Oxide Molecular-Beam Epitaxy Rocks!*, APL Mater. **3**, 062403 (2015).

[6] P.A. Lee, N. Nagaosa, and X.-G. Wen, *Doping a Mott Insulator: Physics of High-Temperature Superconductivity*, Rev. Mod. Phys. **78**, 17 (2006).

[7] M. Choi, F. Oba, and I. Tanaka, *Role of Ti Antisitelike Defects in $SrTiO_3$*, Phys. Rev. Lett. **103**, 185502 (2009).

[8] H.W. Jang *et al.*, *Ferroelectricity in Strain-Free $SrTiO_3$ Thin Films*, Phys. Rev. Lett. **104**, 197601 (2010).

[9] D. Lee *et al.*, *Emergence of Room-Temperature Ferroelectricity at Reduced Dimensions*, Science **349**, 1314 (2015).

[10] E. Abrahams and G. Kotliar, *The Metal-Insulator Transition in Correlated Disordered Systems*, Science **274**, 1853 (1996).

[11] E. Miranda and V. Dobrosavljevic, *Disorder-Driven Non-Fermi Liquid Behaviour of Correlated Electrons*, Rep. Prog. Phys. **68**, 2337 (2005).

[12] K. A. Muller and H. Burkard, *$SrTiO_3$: an Intrinsic Quantum Paraelectric below 4 K*, Phys. Rev. B. **19**, 3593 (1979).

[13] M. Cardona, *Optical Properties and Band Structure of $SrTiO_3$ and $BaTiO_3$*, Phys. Rev. **140**, A651 (1965).

[14] K. R. Udayakumar and A. N. Cormack, *Non-Stoichiometry in Alkaline Earth Excess Alkaline Earth Titanate*, J. Phys. Chem. Solids **50**, 55 (1989).

[15] B. Liu, V. R. Cooper, H. Xu, H. Xiao, Y. Xhang, and W. J. Weber, *Composition Dependent Intrinsic Defect Structures in $SrTiO_3$*, Phys. Chem. Chem. Solids **16**, 15590 (2014).

[16] Y. Kozuka, Y. Hikita, C. Bell, and H.□Y. Hwang, *Dramatic Mobility Enhancements in Doped* $SrTiO_3$ *Thin Films by Defect Management*, Appl. Phys. Lett. **97**, 012107 (2010).

[17] J. Schooley, W. Hosler, and M. Cohen, *Superconductivity in Semiconducting* $SrTiO_3$, Phys. Rev. Lett. **12**, 474 (1964).

[18] O. N. Tufte and P. W. Chapman, *Electron Mobility in Semiconducting Strontium Titanate*, Phys. Rev. **155**, 796 (1967).

[19] A. Ohtomo and H. Y. Hwang, *Growth Mode Control of the Free Carrier Density in* $SrTiO_{3-\delta}$ *Films*, J. Appl. Phys. **102**, 083704 (2007).

[20] R. Viturro, M. L. Slade, and L. J. Brillson, *Optical-Emission Properties of Interface States for Metals on III-V Semiconductor Compounds*, Phys. Rev. Lett. **57**, 487 (1986).

[21] L. J. Brillson, *Interface Bonding, Chemical Reactions, and Defect Formation at Metal-Semiconductor Interfaces*, J. Vac. Sci. Technol. A **25**, 943 (2007).

[22] J. P. Perdew and Y. Wang, *Accurate and Simple Analytic Representation of the Electron-Gas Correlation Energy*, Phys. Rev. B **45**, 13244 (1992).

[23] P. Deak, A. Gali, B. Aradi, and T. Frauenheim, *Accurate Gap Levels and Their Role in the Reliability of Other Calculated Defect Properties*, Phys. Status Solidi B **248**, 790 (2011).

[24] J. Heyd, G. E. Scuseria, and M. Ernzerhof, *Hybrid Functionals Based on a Screened Coulomb Potential*, J. Chem. Phys. **118**, 8207 (2003).

[25] J. Heyd, G. F. Scuseria, and M. Ernzerhof, *Hybrid Functionals Based on a Screened Coulomb Potential*, J. Chem. Phys. **124**, 219906 (2006).

[26] R. Wahl, D. Vogtenhuber, and G. Kresse, $SrTiO_3$ *and* $BaTiO_3$ *Revisited using the Projector Augmented Wave Method: Performance of Hybrid and Semilocal Functionals*, Phys. Rev. B **78**, 104116 (2008).

[27] See Supplemental Material at [URL will be inserted by publisher] for (i) growth of Sr-deficiency-controlled thin films and (ii) finite-size correction scheme for defect simulations, and (iii) fitting of CL spectra.

[28] H. Wang *et al.*, *Stabilization of Highly Polar* $BiFeO_3$*-like Structure: A New Interface Design Route for Enhanced Ferroelectricity in Artificial Perovskite Superlattices*, Phys. Rev. X **6**, 011027 (2016).

[29] R. Dovesi *et al.*, *CRYSTAL14: A Program for the Ab Initio Investigation of Crystalline Solids*, Int. J. Quantum Chem. **114**, 1287 (2014).

[30] P. J. Hay and W. R. Wadt, *Ab Initio Effective Core Potentials for Molecular Calculations. Potentials for the Transition Metal Atoms Sc to Hg*, J. Chem. Phys. **82,** 270 (1984).

[31] S. Piskunov, E. Heifets, R. I. Eglitis, and G. Borstel, *Bulk Properties and Electronic Structure of $SrTiO_3$, $BaTiO_3$, $PbTiO_3$ Perovskites: an Ab Initio HF/DFT Study*, Comput. Mater. Sci. **29**, 165 (2004).

[32] G. Kresse and J. Furthmuller, *Efficiency of Ab-Initio Total Energy Calculations for Metals and Semiconductors Using a Plane-Wave Basis Set*, Comput. Mater. Sci. **6**, 15 (1996).

[33] C. Freysoldt, J. Neugebauer, and C. G. Van de Walle, *Fully Ab Initio Finite-Size Corrections for Charged-Defect Supercell Calculations*, Phys. Rev. Lett. **102**, 016402 (2009).

[34] A. Janotti, J. B. Varley, M. Choi, and C. G. Van de Walle, *Vacancies and Small Polarons in $SrTiO_3$*, Phys. Rev. B **90**, 085202 (2014).

[35] K. van Benthem and C. Elsässer, *Bulk Electronic Structure of $SrTiO_3$: Experiment and Theory*, J. Appl. Phys. **90**, 6156 (2001).

[36] D. A. Tenne, A. K. Farrar, C. M. Brooks, T. Heeg, J. Schubert, H. W. Jang, C. W. Bark, C. M. Folkman, C. B. Eom, and D. G. Schlom, *Ferroelectricity in Nonstoichiometric $SrTiO_3$ Films Studied by Ultraviolet Raman Spectroscopy*, Appl. Phys. Lett. **97**, 142901 (2010).

[37] T. J. Asel, H. Gao, T. J. Heinl, D. Adkins, P. M. Woodward, J. Hoffman, A. Bhattacharya, and L. J. Brillson, *Near-Nanoscale-Resolved Energy Band Structure of $LaNiO_3/La_{2/3}Sr_{1/3}MnO_3/SrTiO_3$ Heterostructures and Their Interfaces*, J. Vac. Sci. Technol. B **33**, 04E103 (2015).

[38] J. Zhang, D. Doutt, T. Merz, J. Chakhalian, M. Kareev, J. Liu, and L. J. Brillson, *Depth-resolved subsurface defects in chemically etched $SrTiO_3$*, Appl. Phys. Lett. **94**, 092904 (2009).

[39] H. Kim, J. Y. Zhang, S. Raghavan, and S. Stemmer, *Direct Observation of Sr Vacancies in $SrTiO_3$ by Quantitative Scanning Transmission Electron Microscopy*, Phys. Rev. X **6**, 041063 (2016).

FIGURE CAPTIONS

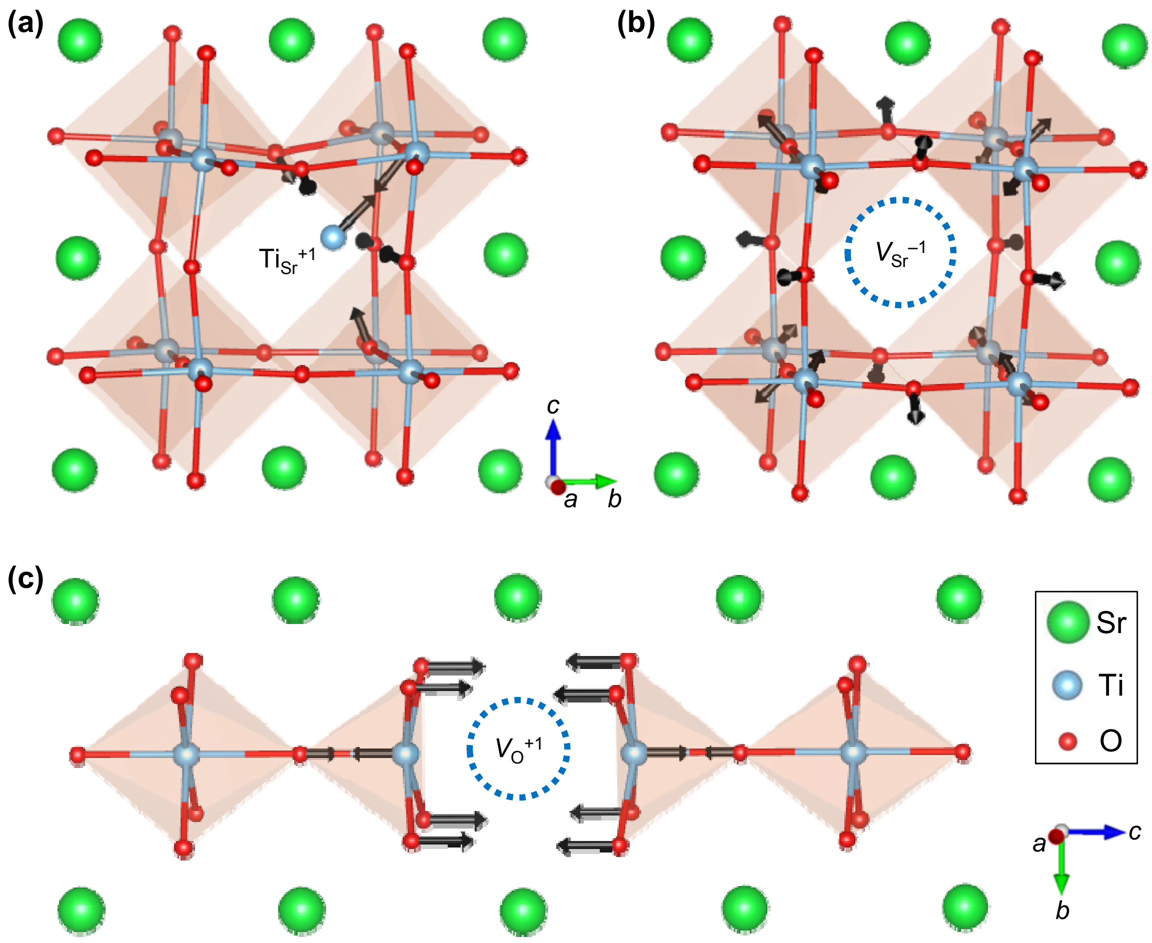

FIG. 1. Atomic structure distortions induced by a point defect. Calculated local atomic structures of $SrTiO_3$ with (a) Ti_{Sr}^{+1}, (b) V_{Sr}^{-1}, and (c) V_O^{+1}. The arrows indicate the directions of the atomic displacement away from the cubic symmetry due to the atomic reconstruction.

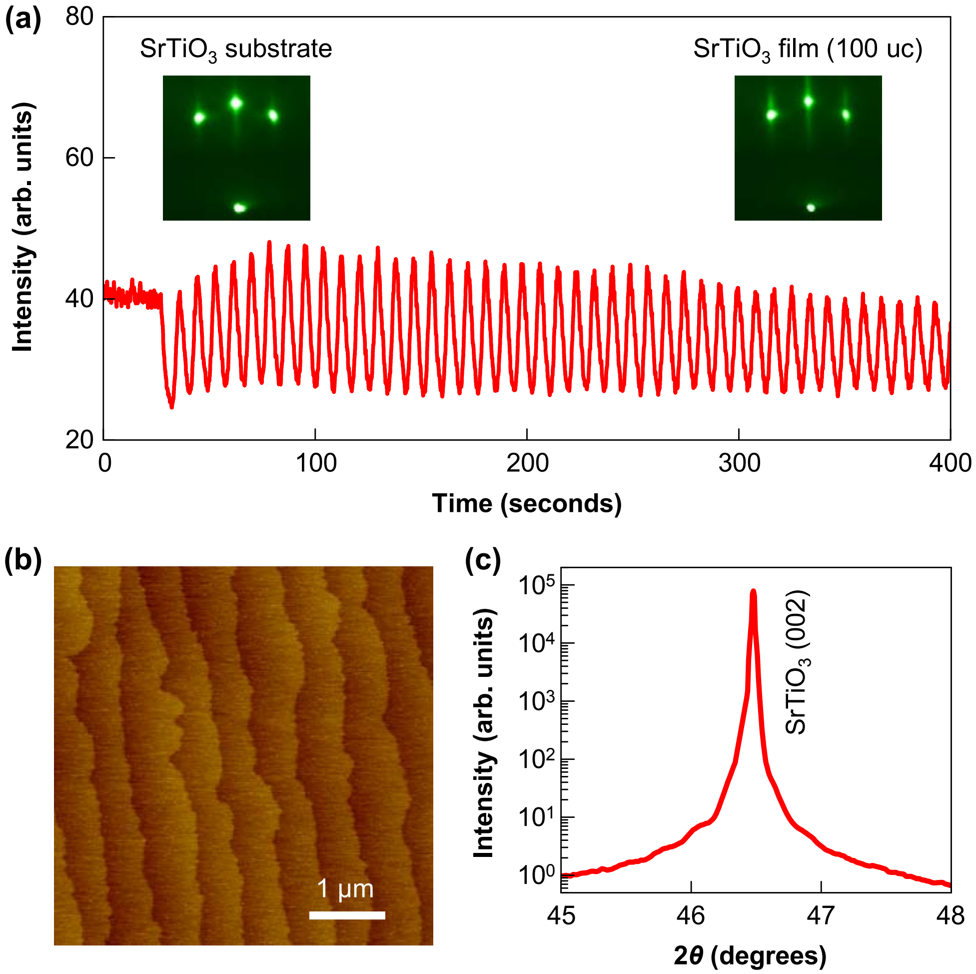

FIG. 2. Growth of homoepitaxial $SrTiO_3$ thin films. (a) RHEED intensity oscillations during growth of $SrTiO_3$ film on $SrTiO_3$ (001) substrate. Insets show RHEED patterns of the $SrTiO_3$ substrate and 100-unit-cells-thick homoepitaxial $SrTiO_3$ film on $SrTiO_3$. 1 unit cell corresponds to 0.3905 nm. (b) AFM image of 100-unit-cells-thick $SrTiO_3$ film, which shows the atomically smooth film surface. (c) XRD θ-2θ curve around the $SrTiO_3$ (002) Bragg peak for 100-unit-cells-thick homoepitaxial $SrTiO_3$ film.

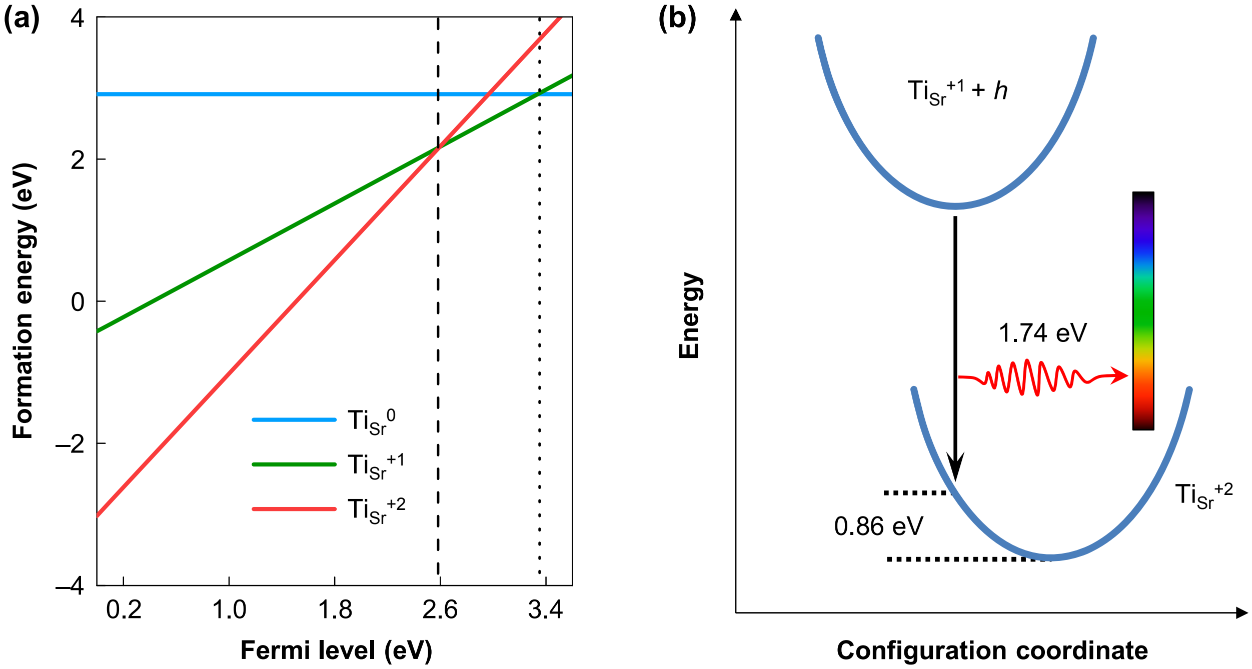

FIG. 3. Microscopic mechanism for luminescence process by Ti_{Sr}. (a) Formation energy of Ti_{Sr} defect of 0, +1, and +2 charge states. (b) Schematic plot of the configuration coordinate diagram for the optical process, $Ti_{Sr}^{+1} + h \rightarrow Ti_{Sr}^{+2}$, which emits photons.

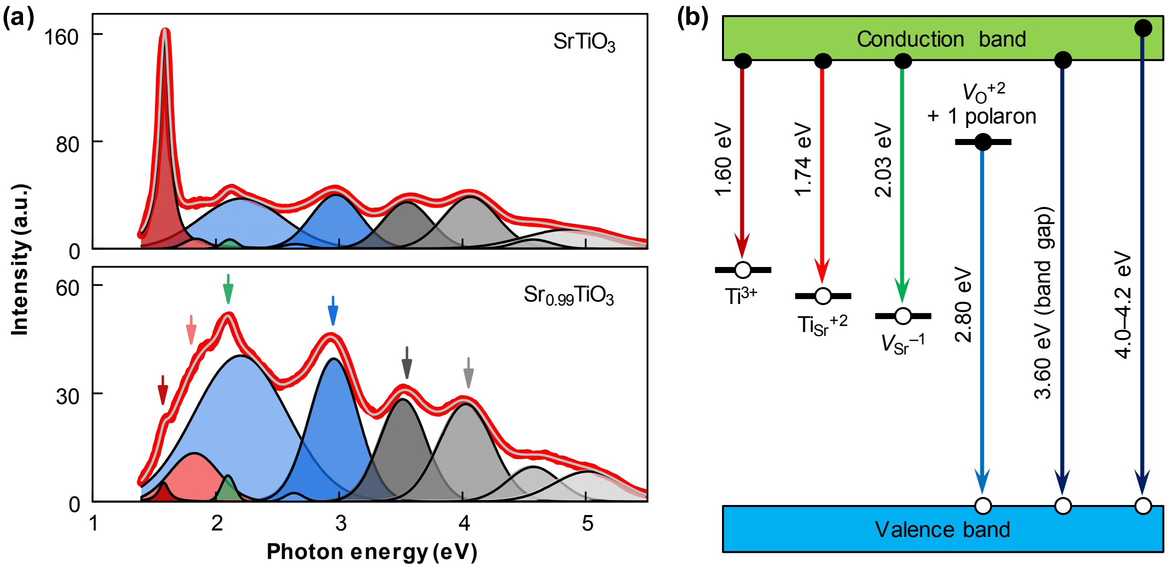

FIG. 4. Point-defect-induced fine structures in the cathodoluminescence (CL) spectra of $SrTiO_3$. (a) CL spectra for 24-unit-cells-thick homoepitaxial $SrTiO_3$ (upper panel) and Sr0.99TiO3 (lower panel) films. The CL spectra are fitted with 9 Gaussian curves (with the centers at ~1.8, ~2.1, ~2.3, ~2.6, ~2.9, ~3.6, and ~4.1 eV, ~4.5 eV, and ~4.9 eV) and one Lorentzian curve (with the center at ~1.6 eV). Six peaks at ~1.6, ~1.8, ~2.1, ~2.9, ~3.6, and ~4.1 are denoted by arrows. Red and gray solid lines indicate experimental and fitted data, respectively. (b) Schematics of luminescence processes. The luminescence by Ti_{Sr}, V_{Sr}, and V_O is predicted from hybrid density functional theory, and the one by Ti^{3+} is from ref. 37.

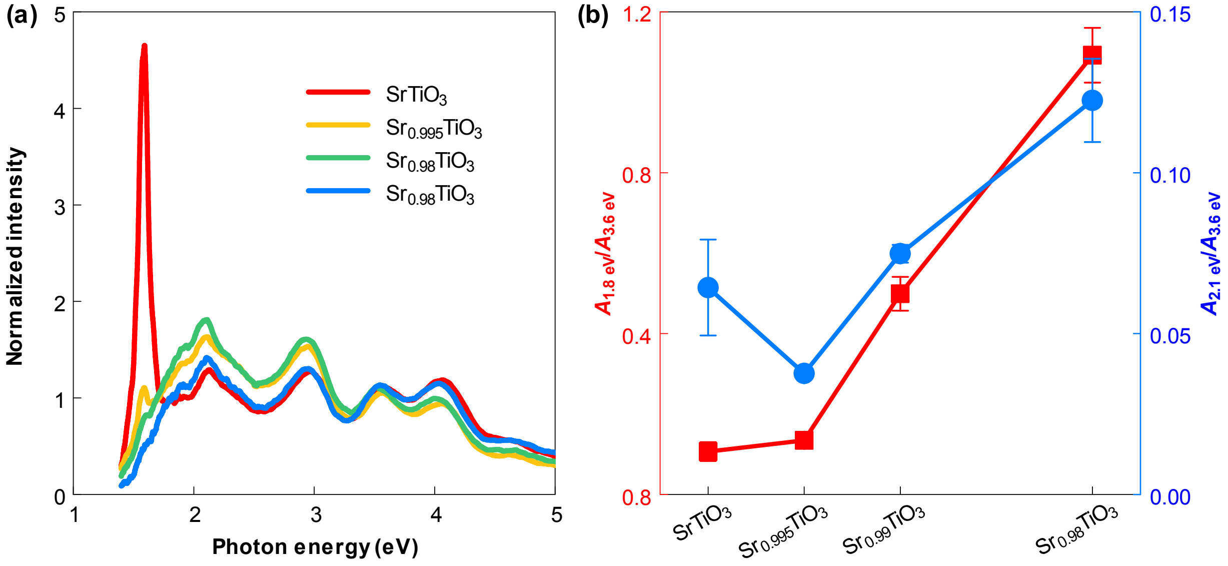

FIG. 5. Identification of point defects by the controlled Sr deficiency in SrTiO$_3$. (a) CL spectra for 24-unit-cells-thick homoepitaxial SrTiO$_3$, Sr$_{0.995}$TiO$_3$, Sr$_{0.99}$TiO$_3$, and Sr$_{0.98}$TiO$_3$ films. We normalize the peak intensity with that of the 3.6-eV CL peak (corresponding to the direct band gap). (b) Areas under the 1.8-eV (red squares) and 2.1-eV (blue circles) CL peaks, normalized with that under the 3.6-eV CL peak, as a function of Sr deficiency.